

## Rapid viscoelastic uplift in southeast Alaska caused by post-Little Ice Age glacial retreat

Christopher F. Larsen<sup>\*</sup>, Roman J. Motyka, Jeffrey T. Freymueller,  
Keith A. Echelmeyer, Erik R. Ivins<sup>1</sup>

*Geophysical Institute, University of Alaska Fairbanks, 903 Koyukuk Dr, Fairbanks, Ak 99775, United States*

Received 16 March 2005; received in revised form 17 June 2005; accepted 27 June 2005

Available online 8 August 2005

Editor: S. King

### Abstract

Our observations show that extreme uplift in southeast Alaska began about 1770 AD, with relative sea level (RSL) change to 5.7 m and current uplift rates to 32 mm/yr. This region experienced widespread glacial melting following the Little Ice Age (LIA), with the collapse of the Glacier Bay Icefield alone equivalent to 8 mm of global sea level rise. Geodynamic modelling links the uplift to post-LIA isostatic rebound, with the extreme uplift signal and a priori knowledge of ice load changes requiring the presence of a low viscosity asthenosphere ( $3.7 \times 10^{18}$  Pa s). These crustal deformations are triggered by climate change through glacier wastage.

© 2005 Elsevier B.V. All rights reserved.

**Keywords:** glacier rebound; glacial isostatic adjustment; Glacier Bay Alaska; glacial wastage; Little Ice Age; sea level variations; mantle viscosity

### 1. Introduction and observations

In southeast Alaska (Fig. 1) we have measured the world's fastest present-day glacio-isostatic uplift yet documented using Global Positioning System (GPS) geodesy combined with studies of raised shorelines. GPS studies of glacier rebound have importance for

deciphering crustal and mantle properties [1]. Glacier rebound affects sea level measurements [2–4], and can lead to increased erosion and therefore additional isostatic effects [5,6]. Furthermore, rebound can affect fault stability [7,8], and release of overburden stress caused by thinning mountain glaciers has increased rates of seismicity in tectonically active southern Alaska [9].

The uplift pattern documented here spans an area of over  $10^5$  km<sup>2</sup>, centered on the coastal mountains along the Gulf of Alaska (Fig. 2A). Tree ring dating of raised shorelines shows that this uplift began only  $235 \pm 20$  yr ago, with relative sea level (RSL) change as much as  $-5.7$  m since then (Fig. 2B).

<sup>\*</sup> Corresponding author. Tel.: +1 907 474 5333; fax: +1 907 474 7290.

E-mail address: [chris.larsen@gi.alaska.edu](mailto:chris.larsen@gi.alaska.edu) (C.F. Larsen).

<sup>1</sup> Jet Propulsion Laboratory, California Institute of Technology, 4800 Oak Grove Dr., Pasadena, Ca 91109.

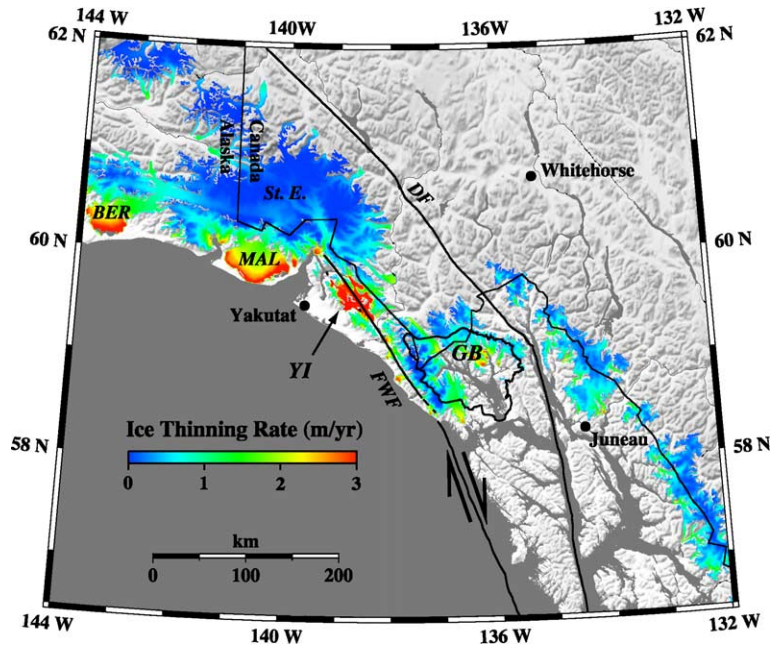


Fig. 1. Location map, showing tectonic setting and present-day glacial wastage. Ice thinning rates follow Arendt et al. [16]. The fastest changes are occurring at lower elevations, such as the termini of the Bering (BER) and Malaspina (MAL) glaciers. The Yakutat Icefield (YI) is an exception to this rule, where thinning rates about three times greater than regional average are driving the greatest ongoing unloading in southeast Alaska. The Glacier Bay Little Ice Age Icefield is outlined (GB). Most of this icefield disappeared over the last ~250 yr. Tectonic deformation along the North America Pacific Plate boundary occurs as strike-slip motion on the Fairweather Fault (FWF), and to a much lesser degree, the Denali Fault (DF). At the northern end of the FWF, crustal shortening accommodates relative plate motion within the St. Elias Mountains (St. E.).

Uplift rates were measured at 72 GPS stations, surveyed primarily in campaign-style 2–5 times each over a 5 yr period (Table 1). These data delineate two separate areas of rapid uplift. The southern peak is centered over Glacier Bay (30 mm/yr) (Fig. 2A). Although in general agreement with earlier estimates of uplift rates based on sea level measurements [10], the density and spatial distribution of our GPS observations provide a vastly improved picture of this uplift. A previously unrecognized uplift peak (32 mm/yr) is centered over the Yakutat Icefield, to the north of Glacier Bay. These peak uplift rates are three times that of GPS uplift rates in Fennoscandia [1] and Hudson Bay [11], where ongoing isostatic rebound has been exponentially decaying since the terminal phases of deglaciation from the Last Glacial Maximum. Acting over a much shorter timescale, similar to that of our observations, historical deglaciation of Iceland following the LIA is driving uplift rates as high as 20 mm/yr as measured by GPS [12,13].

Coastal geomorphology throughout southeast Alaska clearly reveals the long-term effects of this rapid uplift through recent land emergence, new shoals, raised shorelines, and wave-cut benches. We investigated 27 well-defined raised shoreline sites (Fig. 2B). Dendrochronology of Sitka Spruce (*Picea sitchensis* (Bong.) Carr) rooted at the base of the raised shorelines brackets an onset date of 1770 AD ( $\pm 20$  yr) for the current uplift [14,15]. Raised LIA shoreline heights, determined from level-line surveys, are greatest at those sites closest to Glacier Bay and diminish to less than 1.0 m 150 km SE of the Bay, a pattern similar to present-day uplift rates (Fig. 2A and Table 2).

The coastal mountains along the Gulf of Alaska and the Alaskan Panhandle contain around 70,000 km<sup>2</sup> of glaciers and icefields, the world's largest non-polar ice complex. Typically categorized as mountain glaciers, many are adjoining and form large areas of continuous ice coverage over terrain experiencing rapid tectonic motion (Fig. 1). These glacier systems are composed almost exclusively of temperate ice with rapid rates of

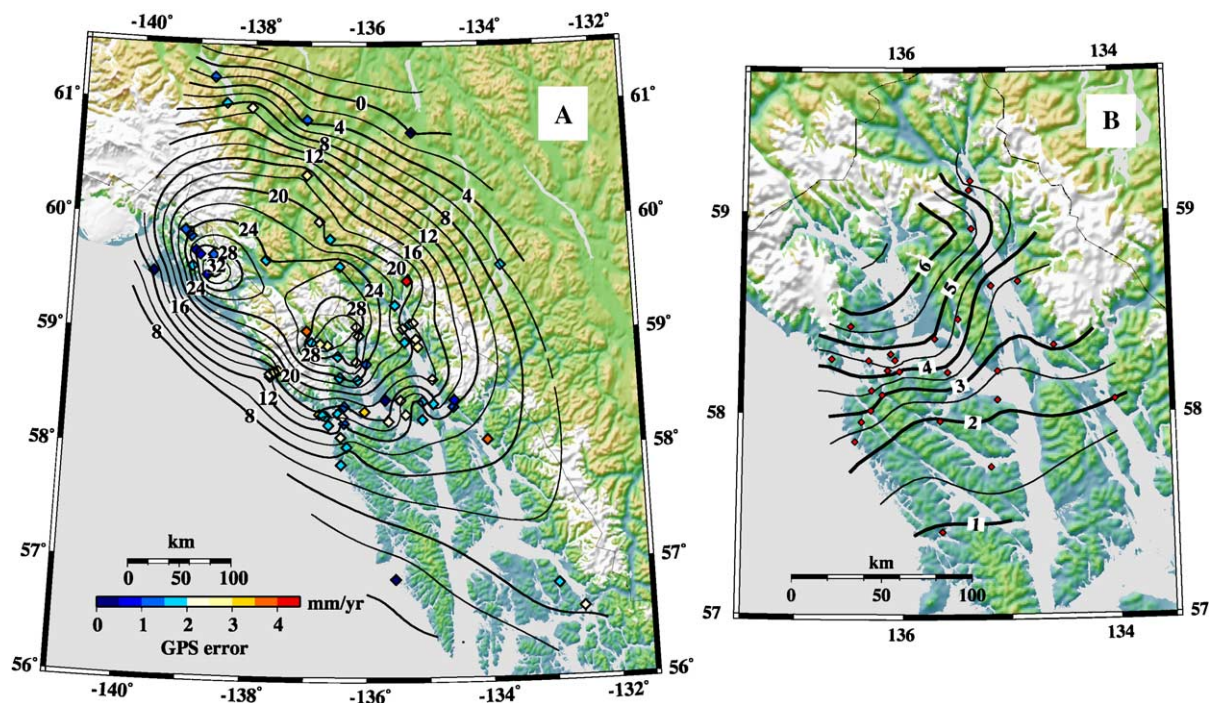


Fig. 2. Uplift observations in southeast Alaska. A) GPS uplift rates (mm/yr). GPS stations are shown with diamonds, colored according to the uplift rate error at each site as indicated by the color scale bar. Contour interval is 2 mm/yr. Peak uplift rates are found in Glacier Bay (southern peak) and the Yakutat Icefield (northern peak). B) Relative sea level change (m). Raised shoreline sites are shown with red diamonds. Contour interval is 0.5 m. At all shoreline sites, uplift was found to have started at AD 1770  $\pm$  20 yr.

mass exchange and so can react rapidly to climatic changes. Airborne laser altimetry measurements throughout Alaska and western Canada show that there has been significant ice volume loss over the last 50 yr, with a regional mass loss rate of 52 Gt  $\text{yr}^{-1}$  from the mid-1950s to the mid-1990's; this has almost doubled to 96 Gt  $\text{yr}^{-1}$  since then [16]. We used laser altimetry measurements [16] to estimate the surface distribution of ice thickness change, including new data (unavailable at the time of Arendt et al. [16]) from the Yakutat Icefield (YI, Fig. 1). Thinning rates in the Yakutat Icefield are roughly 3 times the regional average. Consequently, the region surrounding this icefield is experiencing the greatest ongoing unloading in southeast Alaska.

## 2. What is causing the uplift?

Elastic uplift rates associated with the current ice thinning explain only about 40% of the observed

uplift near the Yakutat Icefield, and 15% in Glacier Bay (Fig. 3). These results indicate that other processes must be driving a significant portion of the uplift in southeast Alaska [17,18,4,15]. Additional contributions to the total uplift signal could arise from tectonic forcing, global glacial isostatic adjustment (GIA), and viscoelastic rebound following post-LIA deglaciation [10,17,18]. Although the active tectonic setting of southern Alaska is fundamentally different than the continental shields of classic post-glacial rebound studies, the tectonic contribution to the geodetic uplift rates is unlikely to be significant relative to the extreme uplift rates observed. For example, in a direct continental collision where tectonically driven crustal shortening is on the order 14–20 mm/yr, the Himalaya exhibits peak geodetic uplift rates of only 3–7 mm/yr [19]. In contrast, the Pacific-North America plate boundary is predominantly strike-slip along the Fairweather Fault (FWF, Fig. 1), and we expect less than a 5 mm/yr tectonic contribution to the

Table 1  
GPS velocities

Latitude	Longitude	Uplift rate (cm/yr)	Error (cm/yr)	Station
–131.59953	55.06907	–0.167	0.010	AIS1
–132.54409	56.59398	0.429	0.233	BLKP
–132.93346	56.80466	0.584	0.194	PSGA
–135.53930	56.85449	0.053	0.018	BIS1
–136.42662	57.85222	0.733	0.187	BLUE
–136.33823	58.00782	0.808	0.195	MINE
–134.01300	58.06755	0.918	0.350	TKHR
–136.43604	58.09134	1.206	0.206	DACE
–136.64098	58.19767	1.340	0.172	CAPE
–136.38090	58.21219	1.152	0.139	ADZE
–135.64497	58.23192	1.606	0.225	EA22
–135.08428	58.24695	1.110	0.175	CLMB
–136.40509	58.26977	1.444	0.202	EX
–136.68720	58.27362	1.283	0.162	NORM
–136.73621	58.28622	1.667	0.173	PEEP
–135.35868	58.28970	1.291	0.211	UDIG
–136.79157	58.29275	1.362	0.318	OVAL
–136.48581	58.29991	1.649	0.179	DEPT
–136.04090	58.31914	1.737	0.331	DAM
–134.56891	58.35633	1.729	0.115	EDDI
–136.37786	58.36018	1.529	0.110	DELT
–134.89978	58.38464	1.578	0.183	TDOG
–135.07598	58.40371	1.162	0.181	RAVE
–134.54525	58.41660	0.900	0.067	MENG
–135.44464	58.41744	1.407	0.221	2437
–135.69748	58.41766	1.733	0.010	GUS2
–136.15285	58.59350	2.424	0.191	ELSE
–134.91064	58.59618	1.837	0.221	BRGT
–136.45710	58.61253	2.358	0.152	KNBG
–137.62046	58.61563	1.568	0.305	2915
–137.57322	58.63984	1.213	0.148	CENO
–137.63186	58.63993	1.304	0.215	FROK
–137.55579	58.65831	1.497	0.267	LITU
–137.51744	58.66329	1.738	0.219	GILB
–137.48888	58.66888	1.866	0.269	ICE4
–136.01446	58.73050	2.372	0.111	BR39
–136.17599	58.74986	2.886	0.200	TLGT
–136.49240	58.79782	2.737	0.178	CINC
–135.14348	58.88208	1.641	0.261	LDDR
–136.66526	58.89277	3.190	0.298	MART
–136.78826	58.90540	3.096	0.262	R205
–136.93206	58.91843	3.089	0.156	SARA
–135.36499	58.92266	2.197	0.187	CAYO
–135.17670	58.94741	2.088	0.234	JA08
–136.14190	58.97887	2.710	0.208	LAST
–137.02025	59.01742	2.665	0.353	MARG
–135.39746	59.04190	1.970	0.202	7SUN
–136.17964	59.05799	3.084	0.226	BAGO
–135.27699	59.08026	1.819	0.179	CHKT
–135.22184	59.09118	1.714	0.234	CKOT
–135.52691	59.24507	2.128	0.174	HNSA
–135.32518	59.45599	2.102	0.406	T187

Table 1 (continued)

Latitude	Longitude	Uplift rate (cm/yr)	Error (cm/yr)	Station
–138.73328	59.49633	3.214	0.071	YAKU
–139.64880	59.51074	1.235	0.043	YKTT
–138.99127	59.56797	2.519	0.167	MOSR
–138.55735	59.57353	3.284	0.168	NOVA
–136.46533	59.58148	2.626	0.172	BEUT
–133.71447	59.58948	0.590	0.158	ATLI
–137.73793	59.63044	2.402	0.197	TATS
–138.86261	59.66928	2.948	0.086	FLAT
–138.63931	59.66985	2.846	0.105	COMB
–138.94546	59.70547	2.842	0.078	HIDD
–136.63489	59.81952	1.864	0.184	TRTH
–139.03155	59.82728	2.354	0.123	NQ4
–139.13489	59.87933	2.428	0.134	NQ1
–136.81893	59.97270	2.059	0.228	489F
–137.05421	60.37623	1.779	0.265	DEZA
–135.22211	60.75051	–0.003	0.010	WHIT
–137.06285	60.85918	0.305	0.125	X7
–138.04046	60.95774	0.953	0.226	LITD
–138.49645	60.99267	0.774	0.153	NSLM
–138.72188	61.21692	0.163	0.140	DEST

The GPS data were analyzed using the GIPSY software with simultaneous data from global International GPS Service (IGS) stations (8). The daily free network solutions were transformed into the International Terrestrial Reference Frame, epoch 2000 (ITRF2000). These daily solutions were used to estimate station velocities that were transformed into a North America fixed reference frame based on the REVEL model (9).

uplift here as summarized in [15]. Beyond the northern end of the FWF, crustal shortening accommodates relative plate motion within the St. Elias Mountains (St. E.). In the St. E., tectonics may be a significant component of uplift rates, and so our comparisons of uplift rates and post-glacial rebound models are focused solely within the strike-slip regime to the southeast. About 5 mm/yr of extension rather than convergence is observed in the horizontal component of the GPS velocities across Glacier Bay. The pattern and distribution of uplift motions in southeast Alaska do not follow faulting geometries here, as would be expected if the uplift were tectonically driven, again suggesting that such forcing along this boundary does not significantly contribute to the broadly distributed uplift signal. Likewise, GIA following Pleistocene continental-scale deglaciations as measured with GPS is on the order of 2–4 mm/yr across much of northwest North America [20]. Accordingly, we concentrate on exploring the effects of a viscous response to recent



Table 2

Relative sea level fall observations at raised shoreline sites

Latitude	Longitude	Relative sea level fall (m)	Error (m)	Site
58.2716	–136.677	4.2	0.3	Graves Harbor
58.4344	–136.5	5.7	0.3	Dundas Bay
57.8595	–136.455	2.3	0.3	Greentop
57.959	–136.393	2.7	0.5	Lisianski Strait
58.2644	–136.327	4.5	0.5	Inian Cove
58.0142	–136.305	3.0	0.3	Bear Creek
58.1155	–136.299	3.6	0.3	Oyster Cove
58.0927	–136.201	3.0	0.3	Idaho Inlet
58.2145	–136.149	4.3	0.3	Gull Cove
58.2973	–136.121	4.8	0.3	North Lemesuir Island
58.2665	–136.078	5.1	0.5	Jacks Cove, Lemesuir Is.
58.2101	–136.038	3.8	0.3	Goose Island
58.3741	–135.705	5.0	0.3	Pleasant Island
57.9612	–135.656	1.9	0.5	Salt Lake Bay
57.4083	–135.637	0.9	0.5	Sulioa Bay
58.2053	–135.583	3.8	0.3	Flynn Cove
58.4716	–135.484	4.4	0.5	Excursion Inlet
59.1144	–135.369	4.8	0.3	Adams Point
59.1592	–135.354	4.2	0.3	Mud Bay
58.9214	–135.35	5.8	0.3	Sullivan Cove
57.7337	–135.182	1.9	0.3	Kadashan Bay
58.6366	–135.166	3.6	0.3	Boat Harbor
58.0679	–135.115	2.1	0.3	Whitestone Bay
58.2125	–135.11	2.5	0.3	Swanson Cove
58.6587	–134.912	3.4	0.5	Echo Cove
58.3404	–134.578	3.1	0.3	9-mile, Juneau
58.0675	–134.013	2.0	0.3	Taku Harbor

unloading following the end of the Little Ice Age (LIA).

### 3. Viscoelastic rebound models

#### 3.1. Earth models

To model the Earth's viscoelastic response to ice load changes in southeast Alaska, we tested a suite of Earth models in which we varied the effective elastic lithospheric thickness and the viscosity profile of the upper mantle while minimizing misfit between the observations and the predicted uplift. We have used two classes of GIA models to calculate the viscoelastic response to ice load changes of glacial advance and retreat through the LIA in southern Alaska. We previously presented models using a gravitating, density stratified, incompressible Earth model consisting of an elastic lithosphere and viscoelastic mantle half-

space [4,15]. The models presented here use a non-rotating, incompressible, self-gravitating, Maxwell viscoelastic, spherically symmetric Earth model [21–23]. Numerically, this model uses axial-symmetric disks to describe surface loads [23], and both the current models and our previously presented models [4,15] use the same surface load geometry. Now, however, we explicitly include a thin, low viscosity asthenosphere, overlaying the upper mantle. The density and elastic properties of the Earth model follow the seismic model PREM. We expanded the spherical harmonics used throughout the numerical modeling to degree and order 1024 in order to resolve small ice load changes and their effects; our regional ice model is gridded at  $20 \times 20$  km resolution. The model calculates both crustal and geoid deformation, and rates thereof.

The earth model parameters that we varied and the ranges over which we varied them are as follows: lithospheric elastic thickness, 30–120 km, astheno-

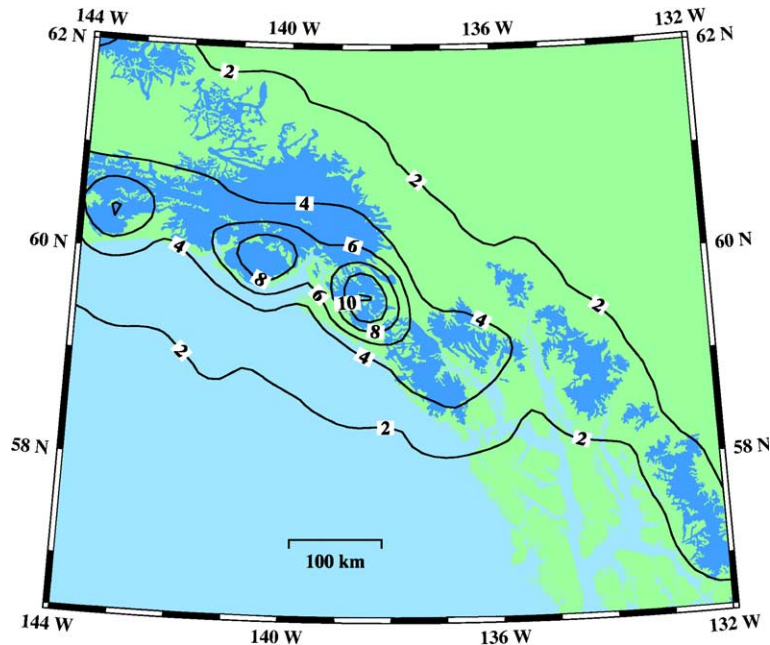


Fig. 3. Elastic only uplift rates (2 mm/yr contour interval).

sphere thickness and viscosity, 80–150 km and  $1 \times 10^{18}$ – $5 \times 10^{19}$  Pa s, and upper mantle viscosity  $1 \times 10^{20}$ – $5 \times 10^{20}$  Pa s. Misfit with the observations was found to rapidly increase at the upper and lower limits of all of these parameter ranges.

### 3.2. Ice load models

These Earth models were subjected to two ice load models simultaneously, one which approximates southern Alaskan and adjoining Canadian glacial history (“Regional”), and one which describes the asynchronous behavior of the Glacier Bay Icefield (“Glacier Bay”). Both of these load histories were held fixed in magnitude and timing for all of the rebound model results presented here. Only the last ~2 kyr of load histories are considered herein.

Although detailed information constrains the timing of advance and retreat of southern Alaskan glaciers [24–26], little quantitative work has been done on estimating regional volume fluctuations over the LIA in southern Alaska. Both land-terminating and tidewater glaciers are found in southern Alaska, with the tidewater glaciers often occupying deep fiords with ice that is many 100’s of meters below sea

level. The volume changes of tidewater glaciers considered herein are restricted to the above sea level changes.

Our regional load model estimates the change in ice volume through the advance and retreat of the LIA [24,25]. The measured rates of volume change [16] were extrapolated to estimate the LIA peak volume in 1900. Earlier volume changes are based on the relative strength of the advance and retreat cycles [25]. We use Neoglacial terminal moraine positions to estimate differential ice volume of these earlier advance and retreat cycles [15], a method that can be problematic in polar systems but is realistic in rapidly adjusting temperate ice systems [27]. The spatial distribution of ice thickness change throughout the load history was allotted according to elevation as in Fig. 1. The distribution of these thickness changes (Fig. 1) are gridded at a  $20 \times 20$  km resolution and assigned a history. This regional ice load model history is based on dendrochronologic and geomorphologic histories of the LIA in southern Alaska [24,25]. The regional ice load model used here is unchanged from Larsen et al. [15].

We account for the large-scale retreat of Glacier Bay in a separate load model (Figs. 4 and 5). The

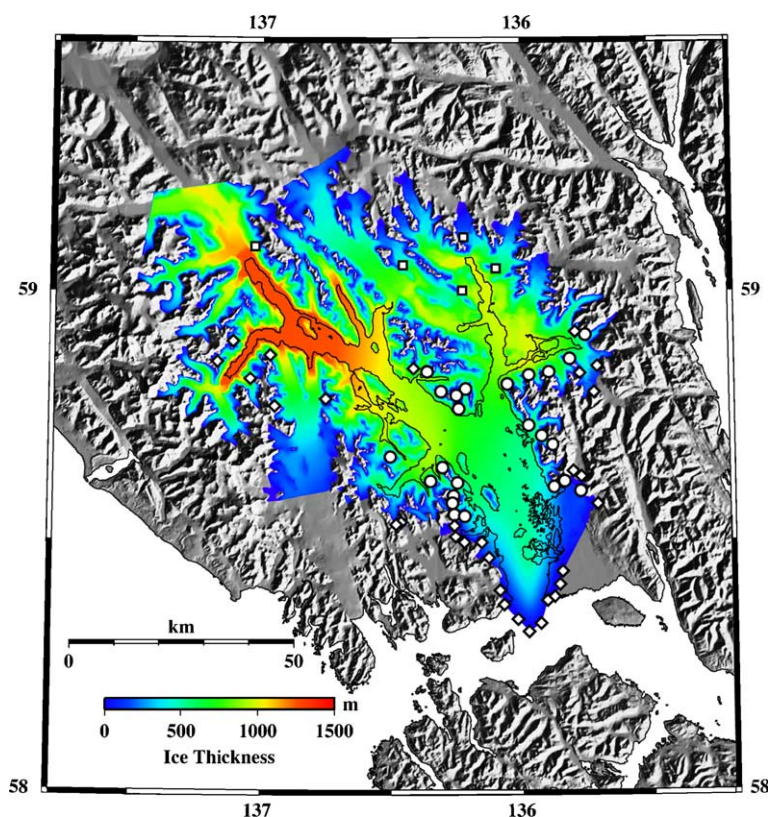


Fig. 4. Ice thickness change in Glacier Bay since the LIA. Total volume of the ice loss is  $3030 \text{ km}^3$ , equivalent to 8 mm rise in global sea level. The modern shoreline in Glacier Bay is outlined beneath the thickness changes. The LIA maximum ice surface was determined by mapping geomorphic markers (trimlines, lateral moraines and terminal moraines). These markers were identified through aerial inspection (circles), vertical airphoto analysis (squares), and high-resolution digital elevation model (DEM) analysis (diamonds). The furthest south three points shown as diamonds are from bathymetric evidence of the LIA terminal moraine. Modern-day glacier analogues were used to construct the GB LIA icefield surface from the geomorphic markers. This surface was then differenced with a DEM of present-day topography to map LIA ice thickness.

Glacier Bay load model invoked herein has several differences from that used in Larsen et al. [15]. Most notably our estimate of the volume of the Glacier Bay LIA maximum extent has increased considerably, based on a greatly improved database and mapping of trimlines, lateral moraines and terminal moraines (Fig. 4). In August 2004, we chartered a small aircraft in Glacier Bay to identify and map these geomorphic markers of the LIA maximum extent from the air. Additional markers were identified from analysis of vertical airphotos and the Shuttle Radar Topography Mission 30 m DEM (<http://seamless.usgs.gov>). These new observations have significantly improved constraints on our model of the LIA Glacier Bay Icefield. We now infer an ice volume loss of  $3030 \text{ km}^3$  from the collapse of this icefield. This localized ice wastage

represents the largest post-LIA deglaciation known to us. Greater than the volume lost from all Alaskan and neighbouring Canadian Glaciers from 1955–2002 [15], it covered a much smaller area with ice thickness changes of up to 1.5 km [28,29]. The volume of ice lost in Glacier Bay alone since the end of the LIA is equivalent to a global rise in sea level (SLE) of 8 mm.

Based on a recent summary of the glacial history of Glacier Bay [30], the timing of the Glacier Bay load model is also modified from our previous models (Fig. 5). First, the large variations in Glacier Bay ice volume during the LIA and before are replaced with a constant load [31] over our  $\sim 2 \text{ kyr}$  load history, with the exception of a rapid advance of the lower bay near the end of the LIA [30]. Secondly, the start of the massive retreat phase at the end of the LIA is later, moved from 1730

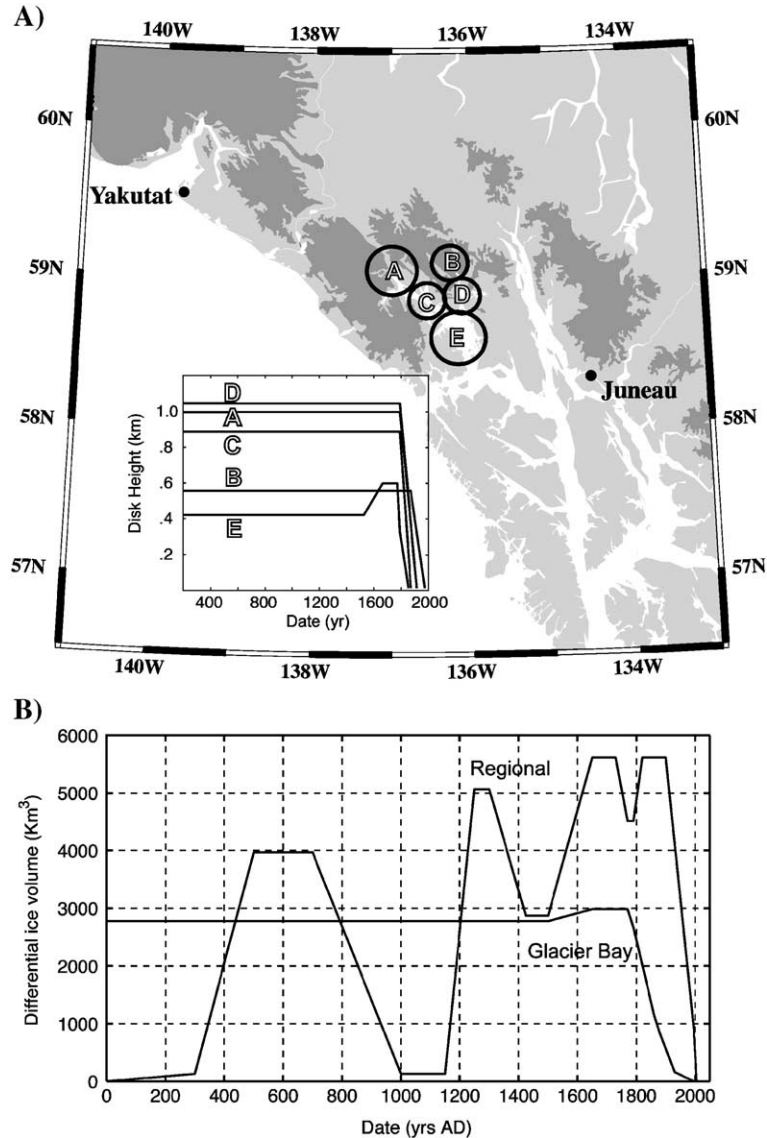


Fig. 5. Ice load models. A) Five disk Glacier Bay load model. Heights of the five disks as a function of time are plotted in the inset. B) Load model histories for the Glacier Bay and Regional load models, as used in the viscoelastic models. The regional load model is distributed over a grid of 531 disks each with 20 km diameter (not shown). This high resolution of the regional load is necessary for accurate modelling of the elastic component. Furthermore, the regional load history includes the recent accelerated wastage starting around 1995 (Arendt et al. [16]).

AD, as was used in our previous models, to 1770 AD, based on dendrochronology [32]. Finally, the rates of unloading during the retreat stages of Glacier Bay (Fig. 5) have been modified to better approximate the effects of drawdown that have been observed in modern temperate tidewater glacier retreats, such as Columbia and Leconte Glaciers, Alaska.

As the Glacier Bay Icefield retreated, seawater inundated the bay. The load change in the newly formed bay caused by seawater replacing the below-sea-level portion of the icefield is accounted for in our models, assuming an ice to water density contrast of 0.917:1. We do not account for the minor seawater loading changes associated with submersion



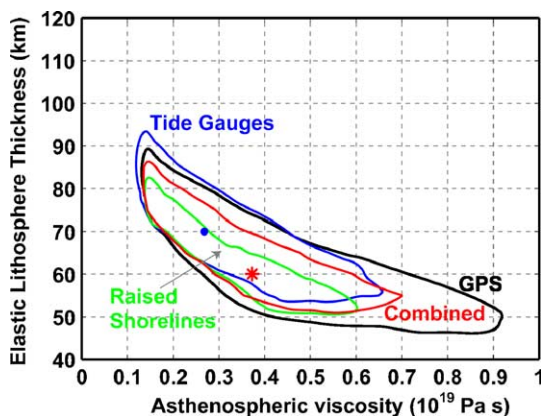


Fig. 6. Rebound model results. The asthenosphere thickness was varied between 80–150 km; the lowest misfits were found for a thickness of 110 km (shown here). Similarly, the upper mantle viscosity was varied between  $2\text{--}5 \times 10^{20}$  Pa s, with the lowest misfits found with  $4 \times 10^{20}$  Pa s (shown here). The contours indicate each best-fit model 95% confidence region. Misfit was evaluated using the reduced chi-square merit function; reduced chi-square is defined as  $\chi_v^2 = \chi^2/\nu$  where  $\nu$  = degrees of freedom. The best-fit models all have asthenosphere viscosity  $3.7 \times 10^{19}$  Pa s and elastic lithosphere thickness 60 km (red star, above), except the tide gauge best-fit model, which has asthenosphere viscosity  $2.7 \times 10^{19}$  Pa s and elastic lithosphere thickness 70 km (blue dot, above). The best-fit models achieved  $\chi_v^2$  values of 1.48 (GPS), 1.27 (tide gauges), 1.63 (raised shorelines), and 1.52 (all data combined). When evaluating the combined dataset misfit, all 119 data points were equally weighted, according to their individual errors, regardless of data type.

and then shallowing of tidelands caused by the isostatic deformation.

#### 4. Model results compared with the observations

Our model assessments are performed through comparisons of model predictions against vertical GPS motions, raised shoreline records of RSL, and also the tide gauge rates of RSL from [4] and [15]. We do not attempt to analyze the horizontal motions resultant from our rebound models here, as has been done in Fennoscandia [1], because the dominant horizontal signal observed in southern Alaska is tectonic. Rather, this will be the subject of a later paper. Error estimation for the raised shoreline measurements was determined from the scatter of repeated measurements of RSL fall at a given site. Errors for GPS and raised shoreline data are listed in Tables 1 and 2. Errors for tide gauge rates follow [4] and [15].

When comparing GPS vertical rates to our rebound models, we assume that the GPS rates solely indicate radial crustal deformation rates. Tide gauge and raised shoreline records of RSL are affected by both geoid deformation and radial crustal deformation, which are both calculated by the numerical rebound models and accounted for in our misfit calculations. Specifically, we approximate RSL as the sum of geoid change, radial crustal deformation and global sea level rise. We use 1.8 mm/yr over the last 120 yr for global sea level rise [33]. When calculating misfit, we use the chi-square statistic [34].

The best-fit models consist of a 60–70 km thick lithosphere, a 110 km thick asthenosphere of viscosity  $2.5\text{--}4.0 \times 10^{18}$  Pa s, over an upper mantle with viscosity  $4 \times 10^{20}$  Pa s. Model results are shown in Fig. 6 for the GPS, tide gauge, and shoreline datasets separately, as well as for a combined dataset. Excellent quality of fit is achieved for each of the three datasets independently, as well as for a combined solution of all the observations. Best-fit  $\chi_v^2$  values are 1.48 (GPS), 1.27 (tide gauges), 1.63 (raised shorelines), and 1.52 (all data combined).

The spatial distribution of misfit is shown in Figs. 7 and 8. When analyzing the spatial misfit distribution across a variety of data types, all with non-uniform errors, it is necessary to consider the error-weighted misfit (Fig. 7). Fig. 7 indicates a generally uniform distribution of weighted misfit, with the exception of an area of outliers in the vicinity of Yakutat. The spatial distribution of GPS uplift rate misfit (Fig. 8B) confirms this area of poor agreement along the northern coastal portion of our study area. Furthermore, the Yakutat tide gauge data had to be omitted from our analysis, as the misfit there was large enough to completely dominate the tide gauge misfit population, preventing a stable best-fit model. The Yakutat GPS site (YKTT), a site with well-determined velocity and an excellent observation history, is also very poorly fit and produces the largest single weighted-misfit value (Fig. 7, inset). In contrast to the tide gauge dataset, the GPS dataset has a much larger population (72 GPS sites vs. 21 tide gauge sites), and the misfit of YKTT does not dominate. Removing YKTT from our analysis improves the overall GPS quality of fit ( $\chi_v^2 = 1.2$ ), but does not change the best-fit model parameters.

The misfit of the Yakutat area is likely due to some combination of tectonics and varying lithospheric

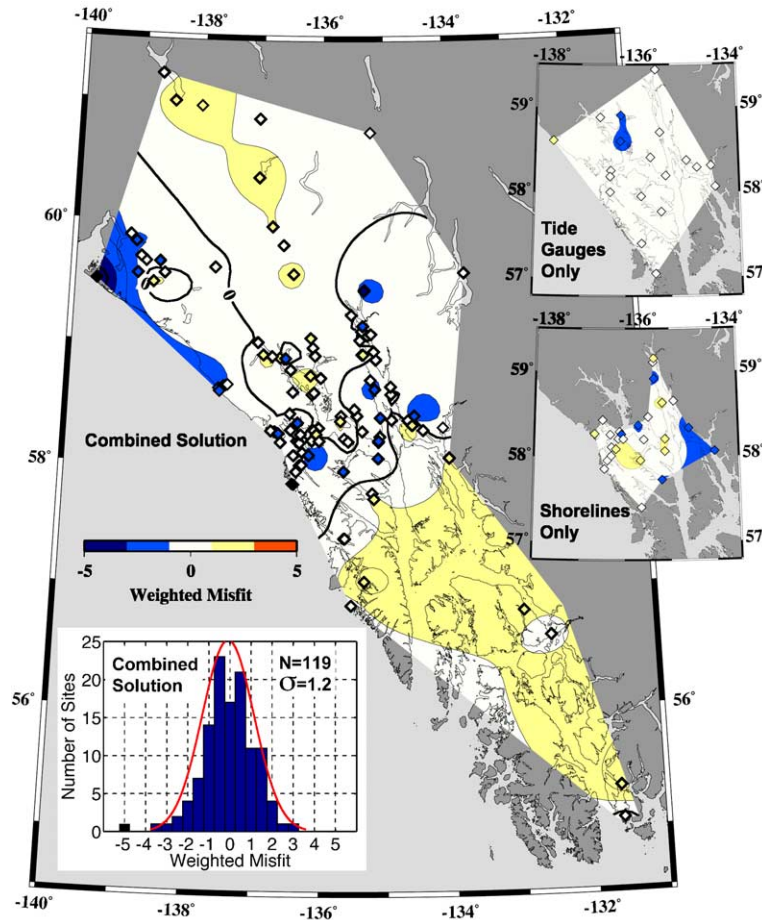


Fig. 7. Misfit distributions. The Earth model consists of a 60 km thick lithosphere and a 110 km thick asthenosphere with viscosity of  $3.7 \times 10^{18}$  Pa s, over an upper mantle of  $4 \times 10^{20}$  Pa s. The main panel maps weighted misfit at all 119 measurement sites. Weighted misfit, shown by the color scale, is the dimensionless quantity calculated by dividing misfit (model minus observation) at each site by that site's error ( $1\sigma$ ). The color scale is used to display weighted misfit at each site (diamonds) as well as on a fitted surface. Note that the large area of positive misfit in the southern portion of the map is constrained by few sites. The two inset maps show the weighted misfit for tide gauge data only and raised shoreline data only. The histogram inset displays the misfit population of the combined solution; this population has a standard deviation of 1.2. The red line plotted over the histogram indicates a normal (Gaussian) distribution over the same range. The  $-5$  outlier on the histogram is the Yakutat GPS site (YKTT).

properties, neither of which are accounted for in our modelling. Yakutat is near where the Pacific-North American plate boundary changes from strike-slip motion to subduction, and the Yakutat tide gauge record indicates some time-varying influence on the uplift rate [4]. Furthermore, this coastal area, bounded to the northeast by the FWF (Fig. 1), is part of the Yakutat Block, a micro-terrane of oceanic and island-arc lithosphere [35]. Indeed, a comparison of the misfit distributions (Figs. 7 and 8) with the location

of the FWF (Fig. 1) suggests that this boundary delineates either lateral variations in Earth material properties, tectonic influences, or some combination of both effects.

## 5. Final remarks

The spatial power spectrum of the combined Glacier Bay and regional load model has peak harmonic

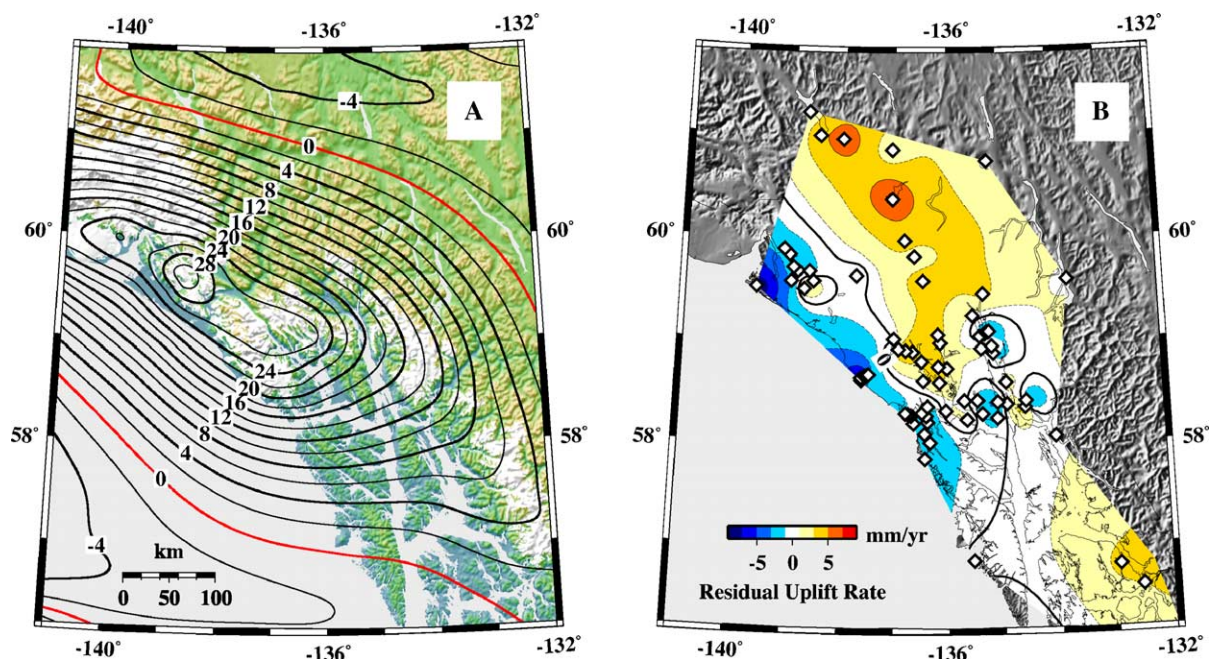


Fig. 8. A) Numerically predicted uplift rates (2 mm/yr contour interval) from the model that produces the best-fit to the GPS data. The Earth model is the same as in Fig. 7. The red contour line (0 mm/yr) indicates the transition from uplift to the subsidence of the forebulge region. B) Residuals between GPS uplift observations (Fig. 2a) and the model predictions shown in panel A, calculated at the GPS sites (shown as diamonds). The distribution of residuals appears to be non-random, and may be correlated with varying crustal structure between the coast and the continent (see text).

load wavelengths in the range of 200–700 km, indicating that the majority of induced rapid flow occurs in the first ~300 km beneath the base of the elastic lithosphere. Our best-fitting models invoke a low viscosity asthenosphere, a model that is generally consistent with other determinations of sub-lithospheric viscosity structure here [4,18] and in other tectonically active regions (e.g., [36–42]). Models of viscoelastic response on centennial timescales are sensitive to trade-offs between load magnitude, load timing and viscosity when mantle viscosities are below  $\sim 10^{20}$  Pa s; above  $\sim 10^{20}$  Pa s the present-day response to such recent changes is almost entirely elastic [3,42]. To invoke the viscous response that the observations require, the viscosity must be low enough to respond to the recent unloading phase. Our constraints on this part of the ice load history are well established, based on eyewitness accounts dating back to 1794 AD [43], which in turn impose solid constraints on the plausible range of earth models.

Our best-fit models indicate that the region has regained about one-half of its LIA subsidence and

predict that another 6–8 m of uplift will occur in Glacier Bay over the next 700–800 yr before achieving gravitational equilibrium, as a result of ice already lost. An oblong forebulge region is predicted roughly 300 km away from Glacier Bay, with present subsidence rates approaching 5 mm/yr (Fig. 8a). The broad dome of uplift over Glacier Bay is a signature of the primarily viscous response to past ice loss there. In contrast, Yakutat Icefield has a significant elastic component that produces the steeper uplift peak at the center of ongoing ice loss (Figs. 2a and 8a), a pattern that should be expected in regions of rapid glacial wastage as the global climate warms. Alaskan glaciers are melting at accelerating rates [16], and large, low elevation termini of coastal glaciers bordering on the Gulf of Alaska are affected greatest by the warming climate. Both the Bering and Malaspina Glaciers (Fig. 1) are likely to have beds below sea level, and the loss of their barrier beachfronts could initiate a rapid tidewater glacier retreat similar to the collapse of Glacier Bay, again leading to massive unloading and rapid crustal deformation.



By combining shoreline uplift data, dated moraine records and precise GPS measurements with viscoelastic rebound modelling, we have linked extreme regional deformation to observations of ongoing massive collapse of LIA glacier systems. The remarkably large amplitude and short timescale of this uplift is evidence that recent changes of glacier systems and ice caps, triggered by climate, can excite a very large solid earth response, much larger than has been previously appreciated. Such flexure can impact regional faulting and seismic activity, and thus has implications for attempts to derive long-term kinematic models and orogenic histories from observations of current crustal movement.

### Acknowledgements

We thank Adam Bucki, Brian Hitchcock, Sigrún Hreinsdóttir, Sandy Zirnheld, By Valentine, Eleanor Boyce, Hilary Fletcher and Ned Rozell for help with extensive field measurements. Glacier Bay National Park and the crew of the R/V Nunatak provided much-appreciated logistical assistance. Anthony Arendt and By Valentine helped with providing recent airborne laser altimetry data. Mike Schmidt and Paul Fluck from the Pacific Geoscience Center provided GPS data from several points in Canada. The National Geodetic Survey provided some of the earlier GPS data in Alaska. We thank G. Spada et al. for making the TABOO rebound program freely available. The figures and most of the ice load model calculations were generated with the Generic Mapping Tools software (<http://gmt.soest.hawaii.edu/>) [44]. UNAVCO provided GPS equipment and data archiving. NASA's Jet Propulsion Laboratory's GYPSY software was used to process the GPS data. This research was funded by the National Science Foundation's EAR Tectonics program and NASA's Earth Systems Enterprise.

### References

- [1] G.A. Milne, J.L. Davis, J.X. Mitrovica, H.-G. Scherneck, J.M. Johansson, M. Vermeer, H. Koivula, Space-geodetic constraints on glacial isostatic adjustment in Fennoscandia, *Science* 291 (2001) 2381–2385.
- [2] B.C. Douglas, Global sea level rise: a redetermination, *Surv. Geophys.* 18 (1997) 279–292.
- [3] M. Tamisiea, J.X. Mitrovica, J.L. Davis, A method for detecting rapid mass flux of small glaciers using local sea level variations, *Earth Planet. Sci. Lett.* 213 (2003) 477–485.
- [4] C.F. Larsen, K.A. Echelmeyer, J.T. Freymueller, R.J. Motyka, Tide gauge records of uplift along the northern Pacific-North American plate boundary, 1937 to 2001, *J. Geophys. Res.* 108 (2003) 2216, doi:10.1029/2001JB001685.
- [5] B. Hallet, L.E. Hunter, J. Bogen, Rates of erosion and sediment evacuation by glaciers: a review of the evidence, *Global Planet. Change* 12 (1996) 213–235.
- [6] J. Jaeger, B. Hallet, T. Pavlis, J. Sauber, D. Lawson, J. Milliman, R. Powell, S.P. Anderson, R. Anderson, Orogenic and glacial research in pristine southern Alaska, *Eos, Trans. AGU* 82 (19) (2001) 213–216.
- [7] R. Arvidsson, Fennoscandian earthquakes: whole crustal rupturing related to postglacial rebound, *Science* 274 (1996) 744–746.
- [8] I.S. Stewart, J. Sauber, J. Rose, Glacio-seismotectonics: ice sheets, crustal deformation and seismicity, *Quat. Sci. Rev.* 19 (2000) 1367–1389.
- [9] J.S. Sauber, B.F. Molnia, Glacial ice mass fluctuations and fault instability in tectonically active southern Alaska, *Glob. Planet. Change* 42 (2004) 279–293.
- [10] S.D. Hicks, W. Shofnos, The determination of land emergence from sea-level observations in southeast Alaska, *J. Geophys. Res.* 70 (1965) 3315–3320.
- [11] J.A. Henton, J.O. Liard, M. Craymer, T. James, C.G. Gagnon, E. Lapelle, Absolute gravity and global positioning system measurements of glacial isostatic adjustment in Eastern Canada, *Eos Trans. AGU* 85 (17) (2004) (Jt. Assem. Suppl., Abstract G41B-02).
- [12] L.E. Sjöberg, M. Pan, S. Erlingsson, E. Asenjo, K. Arnason, Land uplift near Vatnajökull, Iceland, as observed by GPS in 1992, 1996 and 1999, *Geophys. J. Int.* 159 (2004) 943–948.
- [13] H. Geirsson, T. Árnadóttir, C. Völkens, W. Jiang, E. Sturkell, T. Villemin, P. Einarsson, F. Sigmundsson, R. Stefánsson, Current plate movements across the Mid-Atlantic Ridge determined from 5 years of continuous GPS measurements in Iceland, *J. Geophys. Res.* (in press).
- [14] R.J. Motyka, Little ice age subsidence and post little ice age uplift at Juneau, Alaska inferred from dendrochronology and geomorphology, *Quat. Res.* 59 (2003) 300–309.
- [15] C.F. Larsen, R.J. Motyka, J.T. Freymueller, K.A. Echelmeyer, E.R. Ivins, Rapid uplift of southern Alaska caused by recent ice loss, *Geophys. J. Int.* 158 (2004) 1118–1133.
- [16] A.A. Arendt, K.A. Echelmeyer, W.D. Harrison, C.S. Lingle, V.B. Valentine, Rapid wastage of Alaska glaciers and their contribution to rising sea level, *Science* 297 (2002) 382–386.
- [17] J.A. Clark, An inverse problem in glacial geology: the reconstruction of glacier thinning in Glacier Bay, Alaska between A.D. 1910 and 1960 from relative sea-level data, *J. Glaciol.* 18 (1977) 481–503.
- [18] J.S. Sauber, G. Plafker, B.F. Molnia, M.A. Bryant, Crustal deformation associated with glacial fluctuations in the eastern Chugach Mountains, Alaska, *J. Geophys. Res.* 105 (2000) 8055–8077.



- [19] K.M. Larson, R. Bürgmann, R. Bilham, J.T. Freymueller, Kinematics of the India–Eurasia collision zone from GPS measurements, *J. Geophys. Res.* 104 (1999) 1077–1093.
- [20] G.F. Sella, S. Stein, S. Wdowinski, T.H. Dixon, M. Craymer, T. James, Direct constraints on GIA motion in North America using GPS, *Eos Trans. AGU* 85 (17) (2004) (Jt. Assem. Suppl., Abstract G33A-03).
- [21] G. Spada, A. Antonioli, L. Boschi, V. Brandi, S. Cianetti, G. Galvani, C. Giunchi, B. Perniola, N.P. Agostinetti, A. Piersanti, P. Stocchi, Geodesy: modeling earth's post-glacial rebound, *Eos Trans. AGU* 85 (6) (2004) 62.
- [22] G. Spada, A. Antonioli, L. Boschi, V. Brandi, S. Cianetti, G. Galvani, C. Giunchi, B. Perniola, N. Piana Agostinetti, A. Piersanti, P. Stocchi, TABOO, User Guide, Samizdat Press, Golden-White River Junction, 2003.
- [23] G. Spada, *The Theory Behind TABOO*, Samizdat Press, Golden-White River Junction, 2003.
- [24] S.C. Porter, Late Holocene fluctuations of the fiord glacier system in Icy Bay, Alaska, *Arct. Alp. Res.* 21 (1989) 364–379.
- [25] G.C. Wiles, D.J. Barclay, P.E. Calkin, Tree-ring-dated Little Ice Age histories of maritime glaciers from western Prince William Sound, Alaska, *The Holocene* 9 (1999) 163–173.
- [26] R.J. Motyka, J.E. Beget, Taku Glacier, southeast Alaska, U.S.A.: Late Holocene history of a tidewater glacier, *Arct. Alp. Res.* 28 (1996) 42–51.
- [27] W.D. Harrison, C.F. Raymond, K.A. Echelmeyer, R.M. Krimmel, A macroscopic approach to glacier dynamics, *J. Glaciol.* 49 (164) (2003) 13–21.
- [28] W.O. Field, Glaciers of the St. Elias Mountains, in: W.O. Field (Ed.), *Mountain Glaciers of the Northern Hemisphere*, vol. 2, CRREL, Hanover, NH, 1947, pp. 143–297.
- [29] J.J. Clague, S.G. Evans, Historic retreat of Grand Pacific and Melbern Glaciers, St. Elias Mountains, Canada: an analogue for decay of the Cordilleran ice sheet at the end of the Pliocene? *J. Glaciol.* 39 (1993) 619–624.
- [30] C. Connor, W. Howell, D. Monteith, G. Streveler, *Geology and Oral History: Complementary Views of a Former Glacier Bay Landscape*, The 4th Glacier Bay Science Symposium, Oct., 2004, Juneau, Alaska, USGS special pub., in press.
- [31] R.G. Goodwin, Holocene glaciolacustrine sedimentation in Muir Inlet and ice advance in Glacier Bay, Alaska, U.S.A., *Arct. Alp. Res.* 20 (1988) 55–69.
- [32] D. Mann, G. Streveler, unpublished data.
- [33] J.T. Houghton, Y. Ding, D.J. Griggs, M. Noguer, P.J. van der Linden, D. Xiaosu (Eds.), “Climate Change 2001: The Scientific Basis”, Contribution of Working Group I to the Third Assessment Report of the Intergovernmental Panel on Climate Change (IPCC), Cambridge University Press, UK, 2001, pp. 661–663.
- [34] W.H. Press, S.A. Teukolsky, W.T. Vetterling, B.P. Flannery, *Numerical Recipes in C, The Art of Scientific Computing*, Cambridge University Press, Cambridge, 1992, pp. 660–661.
- [35] G. Plafker, L.M. Gilpin, J.C. Lahr, Neotectonic map of Alaska, in: G. Plafker, H.C. Berg (Eds.), *Geology of Alaska, in Decade of North American Geology: Boulder*, Geological Society of America, vol. G-1, 1994, plate 12.
- [36] J.E. Dixon, T.H. Dixon, D.R. Bell, R. Malservisi, Lateral variation in upper mantle viscosity: role of water, *Earth Planet. Sci. Lett.* 222 (2004) 451–467.
- [37] F. Sigmundsson, Post-glacial rebound and asthenosphere viscosity in Iceland, *Geophys. Res. Lett.* 18 (1991) 1131–1134.
- [38] G. Kaufmann, F. Amelung, Reservoir-induced deformation and continental rheology in vicinity of Lake Mead, Nevada, *J. Geophys. Res.* 105 (2000) 16341–16358.
- [39] M. Thoma, D. Wolf, Inverting land uplift near Vatnajökull, Iceland, in terms of lithosphere thickness and viscosity stratification, in: M.G. Sideris (Ed.), *Gravity, Geoid and Geodynamics 2000*, I.A.G. Symposia Series, vol. 123, Springer-Verlag, Berlin, 2001, pp. 97–102.
- [40] D.F. Pollitz, C. Wicks, W. Thatcher, Mantle flow beneath a continental strike slip fault: postseismic deformation after the 1999 Hector Mine earthquake, *Science* 293 (2001) 1814–1818.
- [41] J.J. Clague, T.S. James, History and isostatic effects of the last ice sheet in southern British Columbia, *Quat. Sci. Rev.* 21 (2002) 71–87.
- [42] E.R. Ivins, C.A. Raymond, T.S. James, Late-pleistocene, holocene and present-day ice load evolution in the Antarctic Peninsula: models and predicted vertical crustal motion, in: J.M. Mitrovica, B.L.A. Vermeersen (Eds.), *AGU Geodynamics Ser., Ice Sheets, Sea Level and the Dynamic Earth*, vol. 29, 2002.
- [43] G. Vancouver, *A Voyage of Discovery to the North Pacific Ocean and Round the World 1791–1795*, London, 1798.
- [44] P. Wessel, W.H.F. Smith, New, improved version of the Generic Mapping Tools Released, *Eos Trans. AGU* 79 (1998) 579.